nature biomedical engineering

Article

https://doi.org/10.1038/s41551-024-01183-w

Miniaturized implantable temperature sensors for the long-term monitoring of chronic intestinal inflammation

Received: 28 June 2023

Accepted: 9 February 2024

Published online: 18 March 2024

Check for updates

Surabhi R. Madhvapathy[1,2,12], Matthew I. Bury[3,4,12], Larry W. Wang[5], Joanna L. Ciatti[1,2], Raudel Avila[6], Yonggang Huang[7,8], Arun K. Sharma[3,4,5,9,10] ✉ & John A. Rogers[1,2,10,11] ✉

Diagnosing and monitoring inflammatory bowel diseases, such as Crohn's disease, involves the use of endoscopic imaging, biopsies and serology. These infrequent tests cannot, however, identify sudden onsets and severe flare-ups to facilitate early intervention. Hence, about 70% of patients with Crohn's disease require surgical intestinal resections in their lifetime. Here we report wireless, miniaturized and implantable temperature sensors for the real-time chronic monitoring of disease progression, which we tested for nearly 4 months in a mouse model of Crohn's-disease-like ileitis. Local measurements of intestinal temperature via intraperitoneally implanted sensors held in place against abdominal muscular tissue via two sutures showed the development of ultradian rhythms at approximately 5 weeks before the visual emergence of inflammatory skip lesions. The ultradian rhythms showed correlations with variations in the concentrations of stress hormones and inflammatory cytokines in blood. Decreasing average temperatures over the span of approximately 23 weeks were accompanied by an increasing percentage of inflammatory species in ileal lesions. These miniaturized temperature sensors may aid the early treatment of inflammatory bowel diseases upon the detection of episodic flare-ups.

Inflammatory bowel diseases (IBDs), such as Crohn's disease, affect >7 million individuals worldwide[1]. The global prevalence is highest in Europe/North American countries (~5% annual increase in incidence)[2], with rapid onset and escalation (up to ~15% annual increase in incidence)[3] in the continents of Asia, South America and Africa. Crohn's disease typically results from environmental triggers in genetically susceptible individuals[4] with altered intestinal microflora[5]; up to ~28% of patients have a family history of Crohn's disease[6]. Typically, physical manifestations of Crohn's disease include transmural skip lesions found along the length and circumference of the ileum and the entrance to the

[1]Department of Materials Science and Engineering, Northwestern University, Evanston, IL, USA. [2]Querrey Simpson Institute for Bioelectronics, Northwestern University, Evanston, IL, USA. [3]Division of Pediatric Urology, Department of Surgery, Ann & Robert H. Lurie Children's Hospital of Chicago, Chicago, IL, USA. [4]Stanley Manne Children's Research Institute, Louis A. Simpson and Kimberly K. Querrey Biomedical Research Center, Chicago, IL, USA. [5]Department of Urology, Feinberg School of Medicine, Northwestern University, Chicago, IL, USA. [6]Department of Mechanical Engineering, Rice University, Houston, TX, USA. [7]Department of Mechanical Engineering, Northwestern University, Evanston, IL, USA. [8]Department of Civil Engineering, Northwestern University, Evanston, IL, USA. [9]Simpson Querrey Institute, Northwestern University, Chicago, IL, USA. [10]Department of Biomedical Engineering, Northwestern University, Evanston, IL, USA. [11]Department of Neurological Surgery, Feinberg School of Medicine, Northwestern University, Chicago, IL, USA. [12]These authors contributed equally: Surabhi R. Madhvapathy, Matthew I. Bury. ✉e-mail: arun-sharma@northwestern.edu; jrogers@northwestern.edu

https://doi.org/10.1038/s41551-024-01183-w

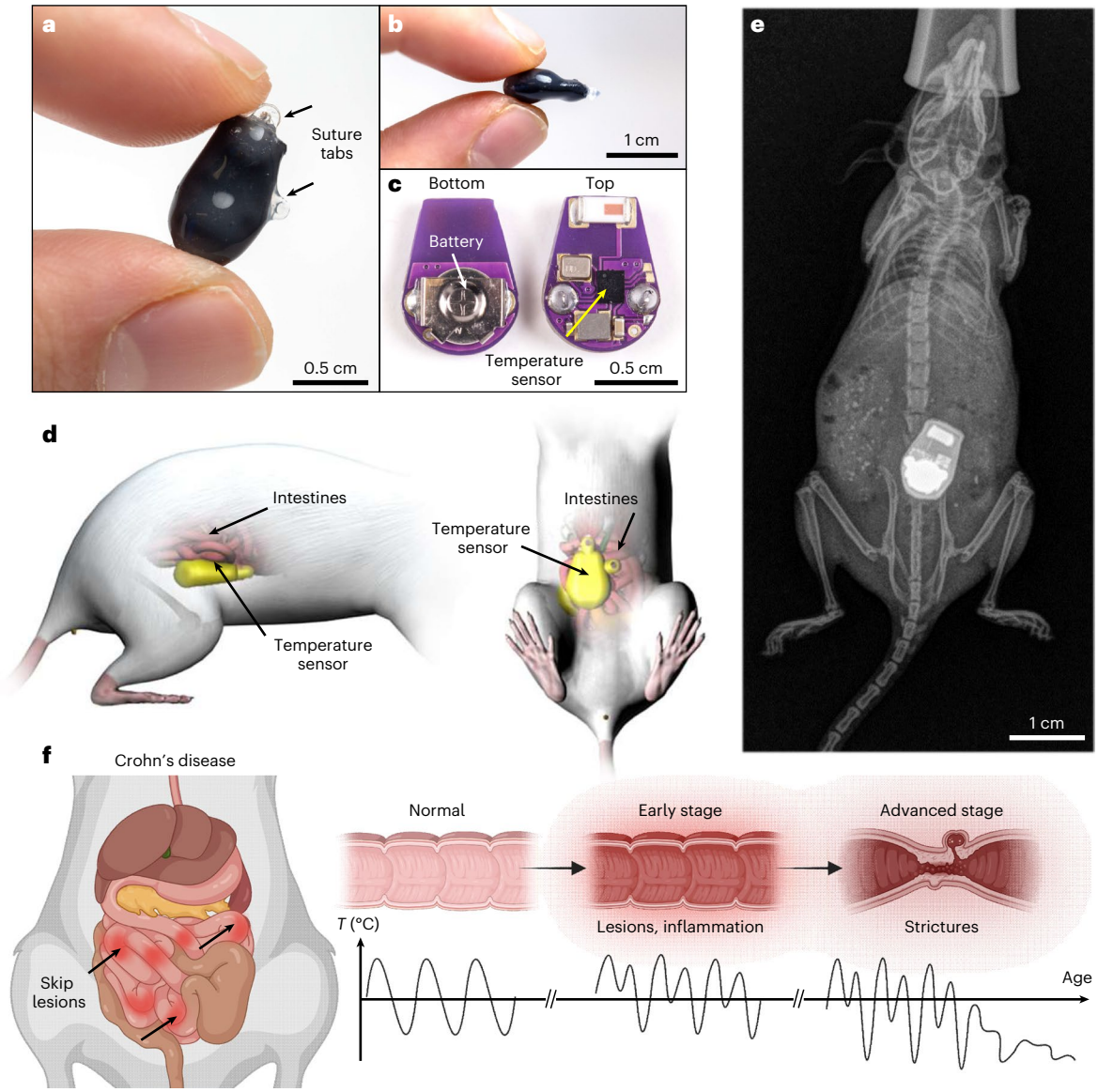

Fig. 1 | Implantable temperature sensors for monitoring Crohn's-disease-like ileitis and their use in studies in mouse models. a–**c**, Top view (**a**) and side view (**b**) of wireless, miniaturized temperature sensors between the thumb and index finger, and of the top and bottom of unencapsulated devices (**c**). **d**, Side- and bottom-view illustrations of a device in a mouse model. **e**, X-ray radiograph of a control AKR/J mouse at 14 weeks of age (~2 weeks after implantation). **f**, Illustration of segmented spontaneous ileitis lesions in the bowel (created with Biorender.com). Sensor measurements capture changes in disease activity as a function of age.

large intestine, containing an overabundant accumulation of innate and adaptive immune cells[5]. Following initial stages of tissue hyperemia[7,8], chronic inflammation destroys intestinal tissue, altering anatomy and physiological function[9–11]. The consequences of moderate/late-stage Crohn's disease include nonspecific symptoms such as severe pain, fever/chills, tissue ulceration and perforation, fistula and fissure formation, bowel obstruction, increased risk of malignant transformation, nutrient malabsorption and subsequent tissue loss[5]. Based upon risk stratification, approximately 70% of patients with Crohn's disease require surgical resection during their lifetime due to uncontrolled and unmonitored flare-ups; 30–60% of these patients require additional surgeries for removal of end-stage tissue at 3–10 years post-initial surgery. Intestinal resection is not curative for Crohn's disease[5,10–12].

Currently lacking is a means to identify and subsequently treat flare-ups associated with ileitis in real time. The average time between diagnosis and the onset of physical symptoms is ~11 years[13]. The gold standard methodology to monitor Crohn's disease progression includes surveillance endoscopy with staging biopsies and downstream pathological assessment. Magnetic resonance imaging and/or computer-aided tomography (CT) and ultrasound imaging complement the endoscopy/biopsy to establish an 'activity index' for Crohn's disease[14–17]. Serology testing accompanies these radiological practices but is nonspecific to Crohn's disease. The long diagnosis/testing times associated with imaging/serology testing (weeks to months), required for determining an appropriate treatment plan, contribute to patient morbidity.

Enhanced strategies to monitor and subsequently treat intestinal inflammation have the potential to prevent additional patient morbidity and the need for surgical intervention. In this Article, we demonstrate chronically implantable, miniaturized, wireless temperature sensors that measure intestinal temperature to detect inflammatory events in real time during progression of a Crohn's-disease-like ileitis in established mouse models[18,19]. Specifically, through chronic (~months)[20,21] implantation and continuous, long-term recordings (up

to ~3.7 months), the data indicate (1) the presence of circadian disruptions and ultradian rhythms (<24 h) in mice with ileitis, correlated with variations in serum concentrations of pro-inflammatory cytokines/anti-inflammatory species/stress hormones and (2) a decrease in the minima associated with daily temperature variations as a function of age, related to histological evidence of deteriorating tissue quality/chronic inflammation over the lifetime of the mouse. The technology presented here may lead to improved treatment approaches for IBDs and enhanced insights into the mechanisms of Crohn's disease.

Results

This study used mouse models with custom-designed sensors that are small (12.8 × 8.2 × 5.8 mm^3 (Supplementary Fig. 1), <1% body volume of ~12-week-old mouse), lightweight (~0.58 g, ~2.3% body weight of 12-week-old mouse) and contoured with smooth surfaces (roughness Sa = 2.8 ± 1.6 μm) for a non-invasive/gentle interface with the intestines, with minimal mass and mechanical load (Fig. 1a–c). The system comprises a bluetooth low-energy system-on-chip (BLE SoC) with an integrated temperature sensor (resolution ~0.01 °C), powered by a coin cell battery (details of the system design, fabrication and calibration procedures in Methods). The combination of size, mass, operating lifetime and measurement accuracy achieved with these devices is unavailable in alternative technologies (Supplementary Table T1).

The design addresses the specific physiological constraints of the intestines, a hollow organ that contains microbiota which influence foreign body responses (FBR)[22]. Abrasion against a large device or one with sharp/rough surfaces and/or introducing sutures into intestinal tissue induces adverse effects such as growth of adhesions, formation of omentum and haemorrhage[23], ultimately leading to strictures and subsequent tissue necrosis in already compromised intestinal tissue for mice with Crohn's disease. Here the intraperitoneally implanted device directly contacts the intestines, held in place against the abdominal muscular tissue with two sutures (through device suture holes). Smooth silicone surfaces (<10 μm roughness) induce minimal immune response[24] and are biocompatible/nontoxic, making them suitable for long-term implantation[25]. Surface roughness measurements are in Supplementary Fig. 2. Details of the procedure are in Methods. The intestines rest naturally over the top surface of the device, enabling free, unrestricted motion during the digestion process (Fig. 1d). Minimal signs of FBR or inflammation appear on the surface of the intestines, the surrounding tissue or other organs even after long-term implantation (Supplementary Figs. 3 and 4). The small device size (Fig. 1e) allows natural locomotor activity, without measurable constraint (Supplementary Fig. 5). Efficient thermal coupling with the intestinal surface enables detection of the presence of Crohn's disease and monitoring of disease severity/progression to identify flare-ups in real time (Fig. 1f).

Experimentation using established mouse models of Crohn's-disease-like ileitis (the SAMP1/YitFc strain)[18,19,26] and their parent strain (AKR/J; non-diseased, no ileitis—which serves as a control) enables detection of Crohn's-disease-associated changes in intestinal temperature ($T_{intestines}$). The studies in Fig. 2 involve implantation at 12 weeks of age, when SAMP1/YitFc mice show full disease penetrance. The time series variation of $T_{intestines}$ of AKR/J mice (representative mouse in Fig. 2a, left) aged between 12 and 16 weeks shows a regular, daily circadian variation, while that of SAMP1/YitFc mice shows pronounced higher-frequency features (representative mouse in Fig. 2a, right). Scalograms derived from wavelet transformation of the time series data in Fig. 2a reveal that SAMP1/YitFc mice have, specifically, strong features at frequencies of $f = 2$, 3 and 4 per day (d^{-1}) throughout the measurement period (Fig. 2b). These ultradian rhythms can occur on the scale of several minutes to several hours, more frequently than the 24 h circadian period[27–29]. Fast Fourier transforms (FFTs) of the data reveal the relative strengths of these >1 d^{-1} rhythms, relative to the $f = 1\ d^{-1}$ circadian rhythm (Fig. 2c). Figure 2d shows the ratios of the amplitudes of these ultradian frequencies ($|X_f|$; $f = 2$, 3, 4 d^{-1}) relative to that of the circadian frequency ($|X_1|$). Ultradian rhythms are nearly absent for AKR/J mice (all $P < 0.0001$, $n = 9$ AKR/J mice and $n = 14$ SAMP1/YitFc mice). Practical applications involving monitoring of Crohn's-disease-associated changes in $T_{intestines}$ would require wavelet transform analysis as a function of time (Supplementary Fig. 6), similar to methods used in other applications[30–32].

On the age scale of 12–16 weeks, the average $T_{intestines}$ and the standard deviation in $T_{intestines}$ ($\sigma_{intestines}$) in AKR/J mice are similar to those in SAMP1/YitFc mice, respectively (Supplementary Fig. 7). An additional sensor placed in the subcutaneous space in the back of the mouse ($T_{subcutaneous}$) reveals that $\bar{T}_{intestines} > \bar{T}_{subcutaneous}$ and $\sigma_{intestines} > \sigma_{subcutaneous}$ for both strains (Supplementary Fig. 8), and $T_{subcutaneous}$ and $T_{intestines}$ show correlations (Supplementary Fig. 9). IBDs, including Crohn's disease, are systemic with both intestinal and extraintestinal manifestations, the latter of which commonly affect the skin and joints[33,34]. Thus, the correlation between $T_{subcutaneous}$ and $T_{intestines}$ suggests the global impact of Crohn's disease on the body and/or could also result from high thermal conductance attributed to the small size and relatively large surface area-to-body mass ratio of the mouse[35,36]. The relationship between the temperatures at these physiological sites merits further study in larger animal models, where considerably large distances separate the dorsal subcutaneous space and the intestines. Finite element analysis (FEA) simulations (Extended Data Fig. 1) illustrate that ultradian rhythms can be captured in mice for most lateral and vertical separations between the sensor and lesions, including at the surface of the skin. In computational simulations for a human, the device would not be able to detect the ultradian rhythms at substantial distances from the intestinal lesions, including the skin surface. This FEA model assumes that inflammatory activity in the lesions is the source of the temperature fluctuations. In the case that the entire core temperature in a large animal shows ultradian temperature variations, an implanted device offers advantages in continuous monitoring over intermittent oral temperature measurements. Continuous, non-invasive measurements of the skin surface overcome the limitations of infrequent monitoring but are subject to influence from ambient temperature, resulting in dampened or unclear circadian oscillations[37]. The environmental temperature in the housing facility shows negligible variation and does not impact circadian or ultradian rhythms in either mouse strain investigated here (Supplementary Fig. 10).

Figure 3 reveals a link between the ultradian rhythms in SAMP1/YitFc mice and relative changes in concentrations of cytokines/hormones, with a dependence on the circadian rhythm. The following analysis specifically focuses on the strongest ultradian feature ($f = 2\ d^{-1}$). Modulation of the light/dark cycle of a SAMP1/YitFc mouse from a 14 h light (6 a.m. to 8 p.m.)/10 h dark (8 p.m. to 6 a.m.) cycle to a 12 h dark (9 a.m. to 9 p.m.)/12 h light (9 p.m. to 9 a.m.) cycle reveals (1) a disruption in the circadian rhythm for ~2 days followed by (2) an ~8 h shift in four specific features of interest: 'peaks' 1 and 3 (local maxima) and 'valleys' 2 and 4 (local minima) (Fig. 3a). Data for the remaining five mice appear in Supplementary Fig. 11. The change in widths of features 1–4 results from the difference in duty cycle of the two light/dark periods. Thus, these four features directly correlate to the circadian rhythm and confirm that they are inherent to SAMP1/YitFc pathophysiology.

Histograms depicting the timing of relative peaks and valleys (determined from a peak-finding algorithm discussed in Methods) over the measurement period show that AKR/J ($n = 8$) mice have a single peak and valley corresponding to nocturnal behaviour; valleys occur at ~1:30 p.m., and peaks occur at ~2:30 a.m., both at the midpoint of the light and dark periods, respectively (Fig. 3b). However, SAMP1/YitFc mice experience an additional local minimum (valley 2 at ~1:30 a.m.) at ~half-way into the dark period before ($n = 25$) (Fig. 3c) and ~70% into the dark period after ($n = 6$) shifting the light/dark cycle (Fig. 3d). Valley 2 appears to 'disrupt' a single circadian peak, creating two distinct

https://doi.org/10.1038/s41551-024-01183-w

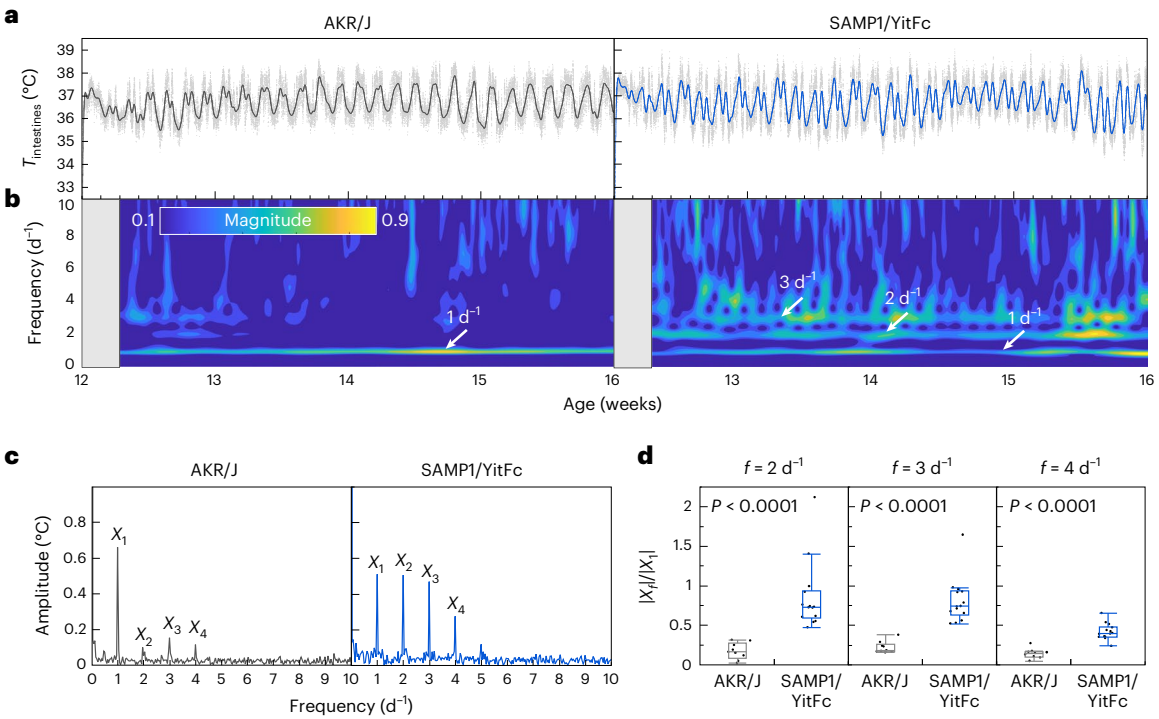

Fig. 2 | Ultradian rhythms in intestinal temperature for mice with spontaneous ileitis. a, Temperature of the intestines ($T_{intestines}$) as a function of age for a representative AKR/J (control) and SAMP1/YitFc (spontaneous ileitis) mouse model. The grey points represent the raw data and the solid line is a spline fit of the data. **b**, Scalograms representing the frequency spectrum of the corresponding time series data in **a**, produced by wavelet transform. The grey box represents the first 0–2 days of data corresponding to post-operative temperature stabilization for which the wavelet transform was not computed. **c**, FFT of the data in **a**. X_f represents the amplitude of the FFT spectrum at frequency f (in d^{-1}). **d**, Box plots representing the ratio of X_2, X_3 and X_4 with respect to X_1 for SAMP1/YitFc (n = 14) mice compared to AKR/J mice (n = 9). The horizontal line within the box represents the sample median and the ends of the box correspond to the interquartile range (first to third quartiles). The whiskers extend beyond the ends of the box by 1.5 × (interquartile range) or to the extreme values of the data (excluding outliers).

peaks (1 and 3) at 8 p.m. and 5 a.m., respectively, in Fig. 3c. In contrast to AKR/J mice, the single valley during the light period (valley 4 in Fig. 3c) occurs ~3 h earlier (at ~10:30 a.m.).

Concurrent expression of several pro-inflammatory cytokines contributes to Crohn's disease immunopathogenesis and disease severity[38–44]. Analysis of key cytokine concentrations in blood, known to play central roles in the progression of Crohn's disease, at valley 2 and peak 3 reveals cyclic inflammatory activity. Specifically, concentrations of pro-inflammatory cytokines in blood including tumour necrosis factor-α (TNFα) and interleukin-1β (IL-1β) (Fig. 3e,f) show higher values at peak 3 compared to valley 2 in SAMP1/YitFc mice, while interferon-γ (IFNγ) and IL-6 show similar trends but are not statistically significant (Fig. 3g,h). Higher serum concentrations of these pro-inflammatory cytokines appear in SAMP1/YitFc mice compared to AKR/J mice. Correlation of TNFα and IL-1β levels with the occurrence of a peak or valley suggests the f = 2 d^{-1} ultradian rhythm in $T_{intestines}$ results from Crohn's-disease-associated inflammatory activity. Understanding the underlying reasons for the f = 3 and 4 d^{-1} rhythms require further study. Feeding cycles, digestion patterns[45] and/or other metabolic processes related to nutrient malabsorption in Crohn's disease[46] are potential explanations.

Investigating concentrations of the adrenocorticotropic hormone (ACTH)—which initiates production of stress hormones such as cortisol and corticosterone—in blood lends insight into the impact of stress on the pathogenesis of Crohn's disease. Measurements of serum concentrations of ACTH in SAMP1/YitFc mice reveal elevated levels (~1.5×) of ACTH at peak 3 relative to those at valley 2 (P < 0.0001) (Fig. 3i), correlating with the f = 2 d^{-1} variation in $T_{intestines}$. ACTH concentrations at valley 2 are ~3.3× higher than light-period concentrations in AKR/J mice (P < 0.0001), suggesting higher overall stress levels in SAMP1/YitFc mice. The cyclic variability in ACTH concentrations and their elevated levels in SAMP1/YitFc mice could be caused by (1) stimulation of ACTH via the gut–brain axis, leading to upregulation of stress hormones[47–49], due to the systemic presence of pro-inflammatory cytokines in the circulating blood and the gut mucosa and/or (2) differences in functionality of bowel movements due to altered presence of intestinal microbiota.

Figure 4 shows the evolution of $T_{intestines}$ for SAMP1/YitFc mice as a function of age beyond the range studied in Fig. 2, over three timeframes (1) before full disease penetrance (<10 weeks), (2) during the early/intermediate stages of ileitis and (3) into the late stages of disease progression (>20 weeks). $T_{intestines}$ for a SAMP1/YitFc mouse aged between 5 and 20 weeks appear in Fig. 4a (data for mice aged until 28 weeks appear in Supplementary Fig. 12). Ultradian frequencies appear before full disease penetrance, starting at ~5 weeks of age (temporal and frequency-spectrum data for additional mice appear in Supplementary Figs. 13 and 14, respectively). At this same time point, gross and microscopic histological appearance of the intestines for SAMP1/YitFc mice is normal[50,51], similar to that of AKR/J mice (Supplementary Fig. 15). This observation suggests that measurements of temperature can reveal early immune responses before the gross manifestation of ileal skip lesions. Previous literature indicates that cytokine levels spike rapidly in these mice well before ~10 weeks of age (between 4 weeks and 7 weeks, known as the 'inductive phase')[18,51]. Thus, measurements of $T_{intestines}$ can indicate the presence of inflammatory activity at least ~5 weeks before visual clinical symptoms appear.

An additional, noteworthy feature in the ~15-week-long data in Fig. 4a is an increase in the daily range of $T_{intestines}$ with respect to age, from ~2 °C at ~5 weeks, to ~3 °C at 12 weeks and to ~4–5 °C after ~18 weeks. This increase in range follows almost entirely from a decreasing daily

https://doi.org/10.1038/s41551-024-01183-w

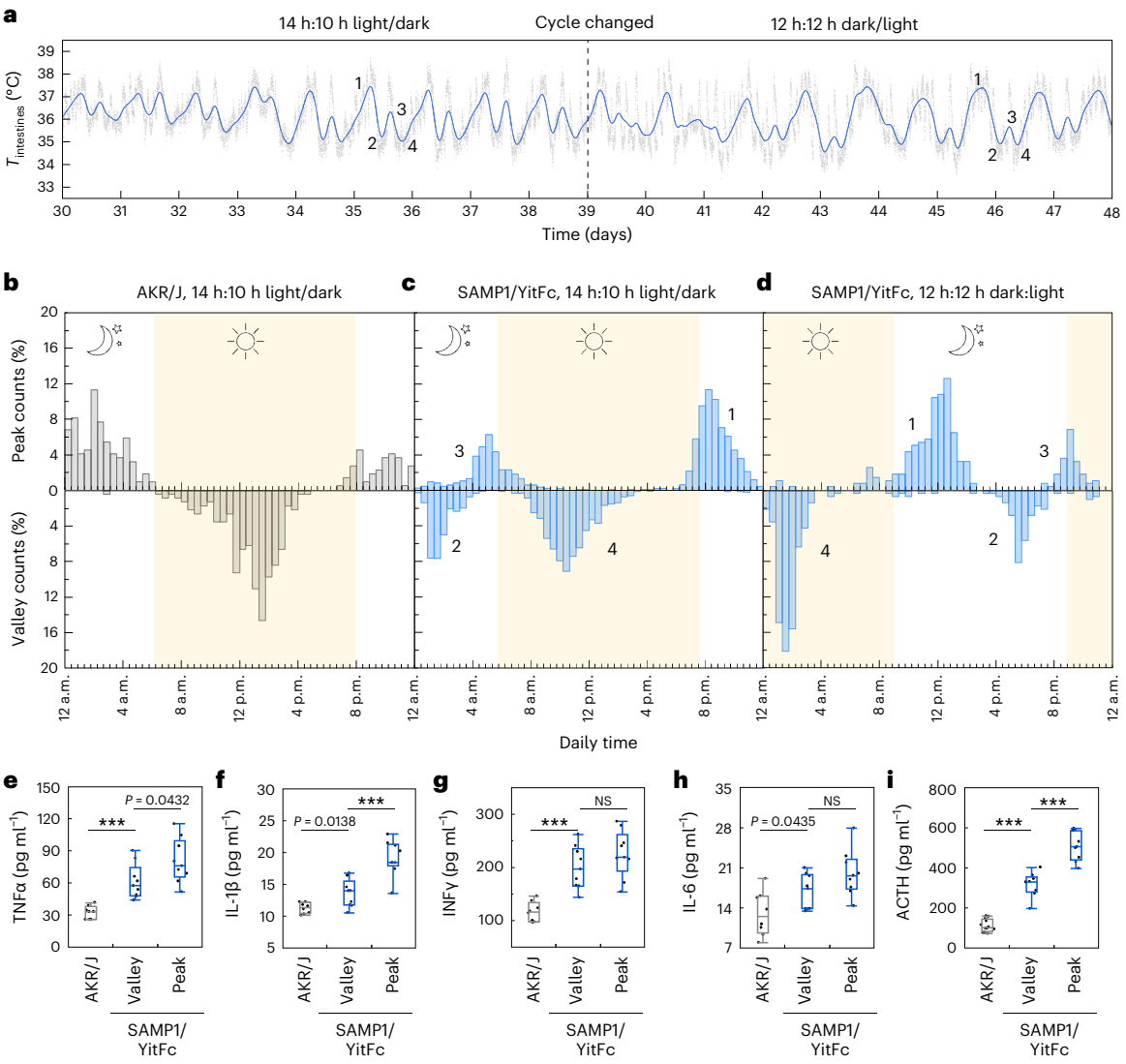

Fig. 3 | Circadian disruptions in temperature for mice with spontaneous ileitis. a, $T_{intestines}$ as a function of time for a representative SAMP1/YitFc mouse undergoing a circadian rhythm modulation between a 14 h:10 h light/dark cycle to a 12 h:12 h dark/light protocol. The two relevant 'peaks' and 'valleys' in the data are labelled 1, 3 and 2, 4, respectively. The grey points represent the raw data and the solid line is a spline fit of the data. **b**–**d**, Histograms illustrating the timings of the peaks and troughs for AKR/J mice ($n = 8$) (**b**), and SAMP1/YitFc mice before ($n = 25$) (**c**) and after ($n = 6$) (**d**) light/dark cycle modulation. **e**–**i**, Serum concentrations of TNFα (**e**), IL-1β (**f**), IFNγ (**g**), IL-6 (**h**) and the ACTH (**i**) of AKR/J mice and SAMP1/YitFc mice collected at temperature valley 2 and peak 3 (**g**). $n = 11$ SAMP1/YitFc per group in **e**–**i**. $n = 8$ AKR/J mice in **e**–**h** and $n = 12$ AKR/J in **i**. $^{NS}P > 0.05$, $^{***}P < 0.001$. For each box plot, the horizontal line within the box represents the sample median and the ends of the box correspond to the interquartile range (first to third quartiles). The whiskers extend beyond the ends of the box by 1.5 × (interquartile range) or to the extreme values of the data (excluding outliers).

minimum from ~36 °C at ~5 weeks of age to 34 °C at 20 weeks of age. The daily maximum remains nearly constant. By contrast, long-term measurements for AKR/J mice show constant average temperature (Supplementary Fig. 16). The decreasing minimum of the daily variation in $T_{intestines}$ in SAMP1/YitFc mice can be attributed to an increased number of lesions (gross histological scoring in Supplementary Fig. 17), lesion sizes (4.65 ± 0.26 mm^2 at 16 weeks, to 6.03 ± 0.5 mm^2 at 28 weeks, $n = 4$) and strictures with age, also resulting in reduced motility with age. Gross histology, motility and lesion sizes are in Supplementary Fig. 18. By contrast, AKR/J mice show good tissue quality and low inflammatory scores even at 20–28 weeks of age.

Microscopic histological analysis of ileal lesions reveals greater inflammatory activity and degrading tissue quality as SAMP1/YitFc mice age. AKR/J mice at 16 weeks of age show normal epithelium and minimal/absence of inflammatory infiltrates (Fig. 4b). SAMP1/YitFc mice, however, show considerable mononuclear cell infiltration in interstitial spaces, a loss of epithelial structure, and thickened mucosa, worsening with age. Inflammatory markers within the tissue, such as TNFα (Fig. 4c), IFNγ (Fig. 4d) and pro-inflammatory macrophages CD68/CD86 (Fig. 4e), are absent in AKR/J intestinal tissue but increase in concentration with age for SAMP1/YitFc mice between 16 and 28 weeks. The increasing $\sigma_{intestines}$ as a function of age (Fig. 4f) correlates with increasing quantitative percentages of these inflammatory markers in the tissue (Fig. 4g). Thus, both long-term (Fig. 4; decrease in daily minimum) and short-term variations (Fig. 3; $f = 2$ d^{-1}) in $T_{intestines}$ link with concentrations of inflammatory cytokines in the tissue and blood, respectively.

Figure 5 illustrates the age dependence and cyclic temporal activity of the peroxisome proliferator-activated receptor gamma (PPARγ) in ileal tissue. PPARγ suppresses inflammatory responses[52], controls circadian variations of blood pressure and heart rate[53] and regulates glucose and lipid metabolism[54,55], playing a key role in IBDs

https://doi.org/10.1038/s41551-024-01183-w

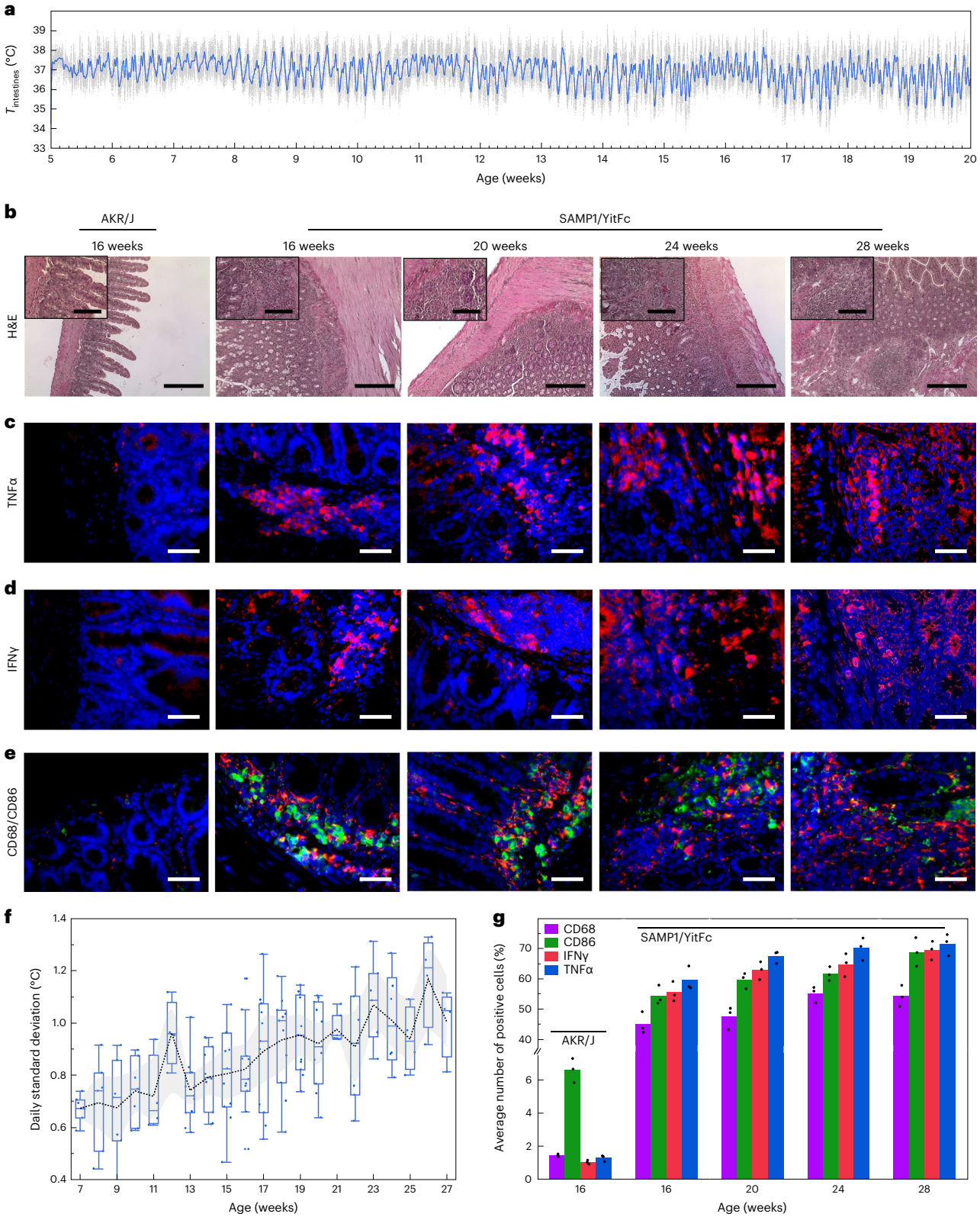

Fig. 4 | Long-term trends in temperature and tissue inflammation. a, $T_{intestines}$ for a representative SAMP1/YitFc mouse aged from 5 to 20 weeks. Device implantation occurred at 5 weeks. The grey points represent the raw data and the solid line is a spline fit of the data. **b**, Haematoxylin and eosin (H&E) staining of affected lesion areas of the small intestine reveals an increase in mononuclear cell infiltration over the time points of 16, 20, 24 and 28 weeks of age for SAMP1/YitFc mice. AKR/J serves as a healthy control. Scale bars, 250 µm, 50 µm (inset images). **c**–**e**, Immuno-fluorescent staining of lesion inflammatory infiltrates shows a steady increase in concentration of pro-inflammatory cytokines TNFα (**c**) and IFNγ (**d**) and an increased presence of macrophages CD68 and CD86 (**e**) from 16–28 weeks of age for SAMP1/YitFc mice. Scale bars, 50 µm. **f**, Daily standard deviation of $T_{intestines}$ as a function of age. $n = 7$ mice for 7–10, 21–24 weeks of age. $n = 4$ mice for 11, 12, 25–27 weeks of age. $n = 11$ mice for 13–15, 17–20 weeks of age. $n = 13$ mice for 16 weeks of age. For each box plot, the horizontal line within the box represents the sample median and the ends of the box correspond to the interquartile range (first to third quartiles). The whiskers extend beyond the ends of the box by 1.5 × (interquartile range) or to the extreme values of the data (excluding outliers). **g**, Quantitative histological evaluation of concentrations of TNFα, IFNγ and CD68/CD86. Error bars represent standard deviations across $n = 3$ animals per age group, 4 lesions per animal and 3 images per lesion.

https://doi.org/10.1038/s41551-024-01183-w

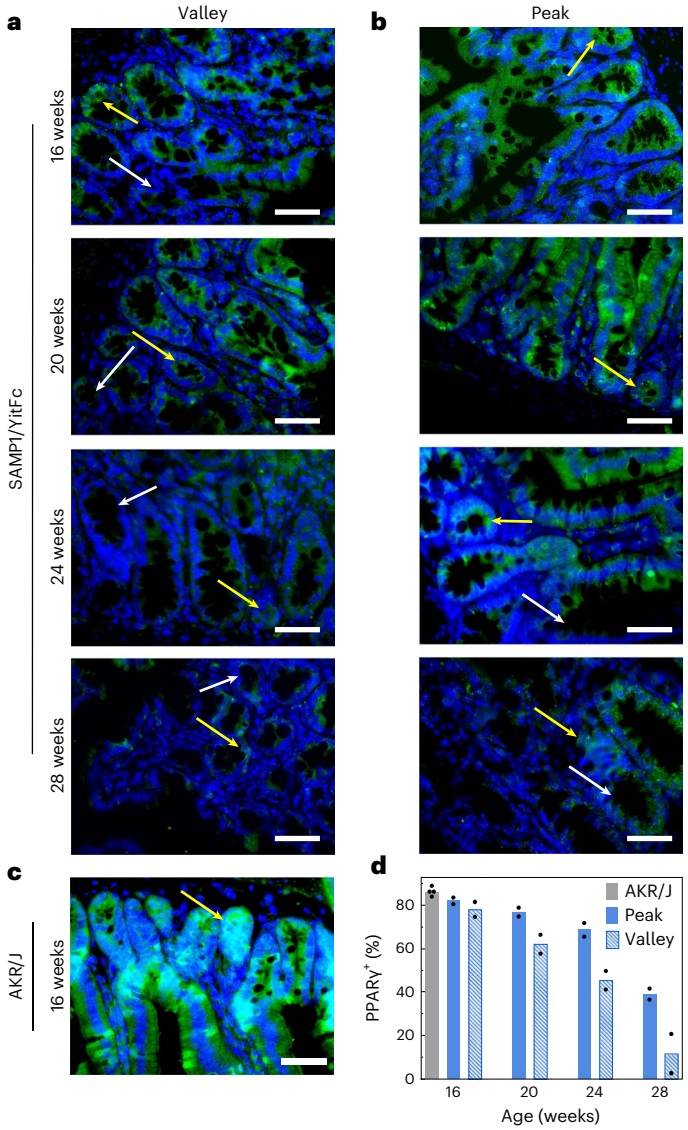

Fig. 5 | Circadian disruptions and influence of aging on PPARγ concentrations in ileal tissue. a–**c**, Immuno-fluorescent staining of ileal tissue of SAMP1/YitFc at valley (**a**) and peak (**b**) time points shows a decrease in positive PPARγ with age and considerably dampened intensity of PPARγ in the crypts and villus when compared to AKR/J mice (**c**). **d**, PPARγ$^+$ staining in SAMP1/YitFc shows a decrease with age in both peak and valley time points. Points represent the average of 10 images per animal, for $n = 4$ animals per age group. Yellow arrows depict PPARγ$^+$ crypts. The white arrows point to crypts that are nearly void of PPARγ. The difference in peak/valley concentrations of PPARγ increases with age. Scale bars, 50 μm.

and metabolic syndromes such as obesity. Qualitatively, PPARγ expression is notably lower in ileal crypts in SAMP1/YitFc mice (Fig. 5a,b) compared to AKR/J mice (Fig. 5c), similar to that observed in ref. 56, and is reduced at valley time points in $T_{intestines}$ relative to those of peaks. Quantitatively, the concentrations of cells which are positive for PPARγ (PPARγ$^+$) in ileal tissue are similar between SAMP1/YitFc and AKR/J mice at 16 weeks of age but subsequently reduce with age for SAMP1/YitFc mice in tandem with the fall in average $T_{intestines}$ with age (Fig. 5d). In addition, the difference in PPARγ$^+$ between peak and valley time points increases with age for SAMP1/YitFc mice, correlating with their $f = 2\ d^{-1}$ rhythms in $T_{intestines}$. These data suggest that the anti-inflammatory effects of PPARγ are deficient in SAMP1/YitFc mice, contributing to disease pathogenesis on both acute (<24 h) and chronic (months) timescales.

Discussion

Continuous, long-term measurements show that features in $T_{intestines}$ correlate with inflammation in mouse models of Crohn's-disease-like ileitis in real time. The time-dependent variations in $T_{intestines}$ reveal ultradian rhythms in mice with Crohn's-disease-like ileitis, compared to normal/control mice, ~5 weeks before the histological emergence of skip lesions. These results offer several important insights into the progression of Crohn's disease over various timescales: (1) within-day ($f = 2\ d^{-1}$) variations and/or circadian disruptions correlate with concentrations of pro-inflammatory cytokines crucial to the pathogenesis of Crohn's disease and ACTH concentrations in blood and (2) variations over months (5–28 weeks of age) associated with aging relate to increasing concentrations of pro-inflammatory cytokines in ileal issue, increasing lesion sizes, strictures and overall tissue quality. Implications for care of patients include prompting the need for additional clinical examination/intervention upon intensified amplitudes in $T_{intestines}$, the need for standardized serology testing during specific times of day, when inflammatory markers in blood show their highest serum concentrations and understanding of efficacy of therapies, and dosing and administration times, as patients with Crohn's disease show wide heterogeneity in response to different medication approaches[57].

Comprehensive study of potential confounding factors, including other inflammatory diseases, other gastrointestinal diseases and systemic conditions on the features in $T_{intestines}$, would enable understanding of the measurement of specificity to Crohn's disease. Pathogenesis of the inflammatory disease osteoarthritis, for instance, shares commonalities with IBD such as gut microbiome dysbiosis and activity of inflammatory species (for example, TNFα and IL-1β)[58,59]. Experimentation on models of osteoarthritis and other conditions could help determine whether the ultradian rhythms and decreasing daily minima are unique to Crohn's disease or are shared with other diseases with similar underlying mechanisms. Our proof-of-concept experiments using a chemically induced model of acute ulcerative colitis, another prominent IBD, in AKR/J mice do not result in ultradian rhythms or the decreasing daily minimum as a function of age (Extended Data Fig. 2). Incorporating other sensors to measure gut motility[60] and/or inflammatory biomarkers[61] could enhance specificity to Crohn's disease; however, currently there are no disease-specific biomarkers of Crohn's disease, and diagnosis involves a combination of endoscopic evaluation and serology testing[62,63]. These biomarkers cannot be used to differentiate between Crohn's disease and ulcerative colitis, while as demonstrated here, measurements of temperature could offer enhanced ability to distinguish between the two diseases. Studies on large animal models[64] would offer insight into the extent of localization of temperature changes to the ileum in Crohn's disease.

External or behavioural factors such as activity/exercise, changes in ambient temperature and changes in food consumption cycles may impact core body temperature and ultimately measurements of $T_{intestines}$. The timescales of these features, however, may allow for differentiation from the ultradian rhythms observed in SAMP1/YitFc mice. Activity/exercise occur on relatively short (45–80 min) timescales[65,66], where body temperature increases at a rate of 0.18–0.25 °C min^{-1} before plateauing during continuous exercise[65]. The rate of temperature change depends on the intensity of the exercise (for example, running speed). Elevated environmental temperatures further increase the magnitude of the temperature change during and post exercise[65]. By contrast, the ultradian rhythms (for example, $f = 2\ d^{-1}$ rhythm) observed in this work for SAMP1/YitFc mice increase and decrease in temperature by ~2.5 °C per 12 h (0.0035 °C min^{-1}). Compared to mice, human T_{core} is less sensitive to a wide range of environmental temperature during exercise. Detecting core body temperature changes as a result of environmental changes can be accomplished through a continuous, non-invasive measurement of ambient temperature from a wearable or other portable device (for example, smartphone). Change in feeding cycles/starvation can also alter core temperatures. After intermittent[67]

or complete starvation[68], core body temperature drops by a rate dependent on extent of starvation (for example, 2.7×10^{-5} °C min^{-1} for rats semi-starved for 9 days receiving only 25% or normal food intake and 6.9×10^{-4} °C min^{-1} for rats starved for 9 days). Ultradian rhythms in temperature are not observed in these cases. These external factors, furthermore, may be infrequent and aperiodic; identification of Crohn's disease activity with highly periodic, ultradian rhythms would require multiple observations of the $f = 2$, 3 and 4 d^{-1} frequencies.

Application in humans requires engineering enhancements to allow data transmission from within the intraperitoneal cavity and to enable wireless recharging of the battery. Endoscopic delivery and securing the device against the intestinal lumen of transmural lesions may present additional guidelines for device design in humans. Envisioned use in humans entails endoscopic insertion of the sensor in the intestines against the luminal wall, without the need for invasive surgical tissue dissection. The video camera at the tip of the endoscope would assist with placement of the sensor against a lesion. Endoscopic insertion of the device would be possible in humans due to the large diameters of the ileum and colon (each 5 cm diameter)[69] compared to mice (0.25 mm and 0.29 mm diameter, respectively)[70]. Tissue adhesives (for example, hydrogels[71] and so on) could secure the device against the intestinal lumen. For implantation in the small intestine, endoscopy may occur by route of the mouth, oesophagus and stomach; engineering considerations would thus require testing of compatibility of the outer encapsulation materials with stomach acids.

Use of this device in patients would be required for (1) initial diagnosis of IBD, (2) assessment of the efficacy of anti-inflammatory therapies, (3) monitoring after surgical resection and (4) continuous monitoring for patients with frequent relapsing of moderate/severe Crohn's disease. The first three cases would require a finite monitoring period. Sensor removal after the desired monitoring period, in these cases, could also occur endoscopically, without the need for additional surgery. Bioresorbable[72] embodiments of the device could be used in very short-term monitoring (weeks to months), as may be required in cases 1 and 3. Sensor implantation in an open surgery such as in case 3 could occur in tandem with another invasive surgery such as intestinal resection, upon identification of adjacent inflamed lesion tissue. While no appreciable FBR appeared on chronic timescales in the mice in this work, further study is required to assess the growth of FBR in larger animal models and in the intestinal lumen.

Outlook

In general, the miniature sizes, wireless communication schemes, low-power operational features, the tissue-compatible form factors and the low-cost manufacturability of the devices reported here suggest wide relevance for study of disease progression in small-animal models and/or other inflammatory disease models. This sort of technology offers a means to capture a rich set of previously unexplored, biophysical information for real-time treatment of IBDs upon detection of episodic flare-ups, to avoid the need for surgical resection.

Methods

Fabrication of miniature, implantable temperature sensors

The sensors consist of a rigid FR4 printed circuit board (PCB), surface mount electronic components, a battery and encapsulation. The design of the two-layer custom PCB made use of Eagle software 9.4.0 (Autodesk). An ISO 9001:2015-compliant vendor (JLCPCB.com) fabricated the devices according to our custom designs using a 0.4-mm-thick FR4 PCB with a solder mask (cover lay) and electroless nickel immersion gold finish on exposed pads. A lead-free solder paste (SAC305 Solder Paste, No-Clean, MG Chemicals) bonded the electronic components, including a BLE SoC and peripherals, to the PCB. Programming of the BLE SoC with custom embedded firmware created using Keil MicroVision (ARM) established the interrupt service routine of the microcontroller. Sampling of $T_{intestines}$ occurred once per minute. The BLE advertising string of each device stored up to five samples of $T_{intestines}$. The BLE advertising string also stored the battery voltage (sampled once every 5 min) and the internal SoC integrated DC–DC converter voltage (sampled every 5 min) to track device battery life/device health. Transmission occurred every 5 min. Installing a 4.8-mm-diameter battery retainer and inserting a coin-cell battery (SR416SW) completed the fabrication process. The battery/operating lifetime was ~10.7 weeks. X-ray radiographs of a mouse implanted with an additional device form factor used in the studies, with a 1-cm-diameter tabbed coin cell battery (CR1025/H9BN), sampling rate of 12 s ($T_{intestines}$), 1 min (battery voltage, DC–DC converter voltage) and transmission rate of ~1 min (containing five samples of $T_{intestines}$) appear in Supplementary Fig. 20. This device form factor had advantages in battery installation and a maximum operating lifetime of ~16 weeks and had no measurable effect on the animal's locomotor activity (Supplementary Fig. 5). Encapsulating the devices in polyolefin provided protection/insulation of the electronics from body fluids. Two suture tabs, cut out from a ~600-µm-thick layer of poly(dimethyl)siloxane (PDMS, Sylgard 184, Dow-Corning) with a CO_2 laser (VLS3.50, Universal Laser Systems) adhered to the polyolefin coating with a silicone adhesive (Sil-Poxy, Smooth-On). Two successive cycles of dip-coating of the device in a low-modulus, fast-cure formulation of silicone (Ecoflex 00-35 Fast, Smooth-On), followed by room-temperature curing of the silicone, formed the soft, smooth protective layer.

Surface roughness measurements

A 3D laser confocal microscope (OLYMPUS LEXT OLS5000) was used to perform surface roughness measurements on the outer device silicone encapsulation. Device preparation before measurement consisted of an isopropanol rinse, drying with a dust-free wipe and removal of residual particulates with adhesive tape (Scotch Magic Tape, 3M). Devices rested on an anti-vibration table under a ×10 objective microscope for profilometry measurements. The LEXT Data Acquisition application enabled collection of stitched images consisting of a 3 × 3 grid over the area of interest on the device. Each individual scan covered an area of 1.635 mm^2 (1,280 µm × 1,277 $µm^2$), and the overall stitched area was 12.77 mm^2. The accompanying LEXT Analysis Application analysed the data with automatic noise cancellation and tilt correction, followed by areal measurement of surface roughness. Averaging five measurements of 0.14 mm^2 area (300 × 300 pixels, that is, 374.1 × 373.8 $µm^2$) per device produced the areal roughness (Sa) for each device. The reported roughness is an average over three independent devices. No filters were applied during roughness measurement.

Calibration of the temperature sensors

All devices underwent calibration before implantation. Calibration involved immersion of the sensors in a uniformly heated water bath (to ~45 °C) and simultaneous recording of (1) the temperature of the bath using a National Institute of Standards and Technology-calibrated thermometer (AO-37804-04, Digi-Sense, Cole-Parmer) and (2) the corresponding analogue-to-digital converter result transmitted by the device, in steps of ~0.5 °C, as the bath cools to ~30 °C. The approximately linear relationship between the sensor analogue-to-digital converter result and water bath temperature defined the calibration curve (examples in Supplementary Fig. 21). No observable signs of temperature drift occur after implantation (Supplementary Fig. 22).

Temperature data collection

A laptop with an open-source serial terminal software (Tera Term Open-Source Project 4) captured and stored the BLE advertising signal in a local text file, as detected by a universal serial bus BLE receiver.

Temperature data processing

Spline fits. Raw temperature data appear as grey dots in all $T_{intestines}$ versus time plots in the main text and supporting information. Smoothing

spline fits appear as dark grey and blue points for AKR/J and SAMP1/YitFc mice, respectively (all with smoothing parameter $\lambda = 0.99$), computed using MATLAB 2022a software.

FFTs and wavelet transforms. FFTs and wavelet transforms required interpolation of $T_{intestines}$ data for cases where the reader did not capture a transmission event. The fraction of data dropouts is typically 0.01% (Supplementary Fig. 23). Analysis excluded the first 2 days of data post operation. Wavelet transforms were computed with 48 voices per octave. Both transforms were computed using MATLAB 2022a software.

Moving standard deviation. Moving standard deviations (window = 1 day) required interpolation of $T_{intestines}$ data for cases where the reader did not capture a transmission event. Analysis excluded the first 2 days of data post operation. Each point reported in Fig. 4f represents the daily standard deviation per week per mouse.

Peak–valley histograms. Peak–valley analysis conducted on the spline fit of the data revealed the timings of the features in the $f = 2\ d^{-1}$ rhythm. Custom MATLAB software identified local minima and maxima in the spline fit. Histograms of the timestamp at which peaks/valleys occurred show peaks/valleys with magnitude ≥0.7 °C (plotted with JMP Pro 16 software). The first 2 days of data post operation were excluded from analysis.

Mice
Female SAMP1/YitFc mice (The Jackson Laboratory) aged 4–20 weeks and female AKR/J mice (The Jackson Laboratory) formed the experimental and control groups, respectively. The Institutional Animal Care and Use Committee at Northwestern University's Center for Comparative Medicine approved all animals and procedures before experimentation (IS12661).

Surgical implantation procedure
A portable induction chamber and gas inhalation system (IMPAC6 Integrated Multi-Patient Anesthesia Center, VetEquip) providing 2% isoflurane in oxygen delivered anaesthesia to animals before surgery. Once asleep, injection of buprenorphine 0.05 mg kg^{-1} and meloxicam 2 mg kg^{-1} between the shoulder blades of the animal provided analgesia. The next step involved shaving the fur on the abdomen. Application of T-Bact 2% mupirocin ointment (Glaxo SmithKline Pharmaceuticals) disinfected the targeted incision area of the abdominal skin. A ~1 cm midline incision created in the skin and muscle areas exposed the abdominal cavity. Sensors were disinfected with ethanol immediately before insertion into the abdominal cavity. The temperature-sensor side of the device interfaced with the intestines, and the battery side contacted the abdominal muscle tissue. Then 4–0 polydioxanone sutures (Ethicon) secured the two device suture tabs to the abdominal muscle; 4–0 polydioxanone sutures then closed the muscle. As a final step, 4–0 nylon sutures (Ethicon) closed the skin.

Post-operative care and housing
A heating pad at ~35 °C underneath half of the animal cage provided support for body temperature regulation for ~48 h post surgery. Animals were housed in a barrier facility for immunocompromised animals with a regular 14 h:10 h light/dark cycle and had access to standard laboratory chow and water ad libitum. Animals with a single implant in the abdominal cavity were housed in pairs, and those in Supplementary Fig. 8 with one implanted sensor in the abdominal cavity and one implanted sensor in the dorsal subcutaneous space were housed individually.

Enzyme-linked immunosorbent assays
Sample preparation involved collection of whole blood (400–500 µl) of each individual animal at the experimental endpoint, followed by coagulation at room temperature and centrifugation at 1,000 *g* for 10 min. Samples collected for $n = 8$ AKR/J mice and $n = 11$ SAMP1/YitFc mice at a temperature peak, and $n = 11$ SAMP1/YitFc mice at a temperature valley allowed testing for the concentrations of the ACTH (Abcam), TNFα, IFNγ, IL-6 and IL-1β (Sigma-Aldrich) using enzyme-linked immunosorbent assays conducted according to vendor instructions. All enzyme-linked immunosorbent assays utilized a ~1:2 dilution of serum.

Motility experiments
Motility experiments followed the procedure in ref. 19. Water-only fasting of the animals occurred 6 h before the procedure. The next step involved administering an oral gavage dose of 100 mg ml^{-1} fluorescein isothiocyanate–dextran (in saline; 44 mg per 100 g body weight; 70,000 MW, Sigma Aldrich). After 1.5 h, the animals were euthanized, and the entire intestinal track was removed. Separation of the small intestine into ten sections, the cecum into one section and the colon into three sections allowed for evaluation of motility at specific locations. Exactly 1 ml of Kreb's solution cleared individual sections which were then collected into single Eppendorf tubes. Centrifugation of subsequent samples allowed for collection of the supernatant. A 96-well plate reader determined total accumulation of fluorescein isothiocyanate–dextran in individual sections.

Radiograph collection
Radiograph collection relied on a portable radiograph collection system (Slatehub, Veterinary Cuattro Slatehub, Heska) on animals anaesthetized under 2% isoflurane, ~2 weeks after device implantation in AKR/J mice at ~14 weeks of age. Image acquisition occurred with setting exposure factors of 60 kVp, 5 mAs, and 40 mA.

Light/dark cycle modulation experiments
Transporting animals initially housed in a 14 h light/10 h dark room (6:00–20:00 lights ON) to an adjacent room with a 12 h dark/12 h light cycle (9:00–21:00 lights OFF) on day 39 post surgery allowed for disruption/modulation of the circadian rhythms of the animals. All other conditions (room temperature, food/water availability and so on) remained constant.

Preparation of histological samples and staining
Histological sample preparation, analysis and immunohistochemistry followed the procedures in ref. 19. Collection of other soft tissues (heart, liver, lung, spleen kidney, small intestine and large intestine) followed serum collection and motility experiments. Calipers (Mitutoyo Absolute Digital Caliper) enabled measurements of lesion size in the ileum (length and width of individually affected tissue areas) of SAMP1/YitFc mice. The next steps involved fixing the collected tissue in a 10% buffered formalin phosphate for 24 h, subsequent dehydration utilizing graduated ethanol solutions, clearing with xylenes and finally embedding the tissue in paraffin wax. Construction of moulds, followed by sectioning onto glass slides, completed the sample preparation process. Haematoxylin and eosin staining was used to stain the slides.

Immunohistochemistry
Prepared tissue section slides were placed in boiling antigen retrieval buffer (0.01 M citrate, pH 6.0, 0.05% Tween-20) for 15 min and were then cooled to room temperature. Bovine serum albumin (BSA, 5 mg ml^{-1}) (Sigma-Aldrich) blocked the slides for 15 min, with the subsequent addition of primary antibodies (Abcam (MA, USA) for inflammatory markers and cytokines (TNFα, IFNγ, CD68, CD86 and PPARγ) to tissue sections. Primary antibodies were utilized at a dilution of 1:100. Following a 1 h incubation, phosphate-buffered saline was used to wash the slides, followed by incubation with fluorescent secondary antibodies diluted at 1:400 (Invitrogen) for 30 min. An additional saline wash and subsequent mounting of Vectashield with a 4′,6-diamidino-2-phenylindole additive onto the slides (Vector Laboratories) completed the process.

Histological analysis

Quantitative scoring. Images of affected ileal tissue sections (four areas per animal with three images per area for TNFα, IL-1β, CD68, CD86 and ten images of the epithelial tissue per animal for PPARγ) were taken utilizing a Nikon Eclipse 50i microscope and Spot Advanced Imaging software (SPOT 4.0). Quantification of positively stained tissue sections involved manually counting fluorescently stained cells using ImageJ (IJ 1.46r) cell counter plugin function (National Institutes of Health). The ImageJ software determined the total number of cells in each image by changing the image threshold to only feature 4′,6-diamidino-2-phenylindole-positive cells (DAPI). The watershed function removed stacked cells. Application of the analyse particle tool with the size adjusted to 50–200 pixels and circularity set to 0.0–1.0 completed the process.

Qualitative scoring. Three blinded participants conducted segment gross pathology scoring. The small intestine was separated into 10 sections with scores ranging from 1 being no lesion/affected area with no visible stricture to 5 being multiple structures with multiple affected lesion areas of the segmented area. Both quantitative and qualitative analyses were blinded.

Video analysis

Video collection occurred ~7 days post operation at ~6:30 a.m. Animals paired with their cage mate temporarily relocated to clean, open-top, lidless cages with bedding only (without other enrichment). Top-down camera recording using a day/night (infra-red) vision webcam occurred for ~15 min. Animals were then returned to their original cages. Utilization of DeepLabCut 2.3 software allowed for quantification of motion.

Dextran sulfate sodium-induced colitis model

To produce an acute colitis model, AKR/J mice at 10 weeks of age received a temperature sensor implant. Following a 2 week recovery period, animals received treatment to induce colitis. This treatment consisted of the addition of 1–5% dextran sulfate sodium (DSS) in the drinking water of animals for 7 days, followed by normal water for 7 days. This cycle was repeated for the cases of 1% and 3% DSS. Animals subject to 5% DSS treatment only underwent one 7 day cycle as they experienced a >20% body weight change along with bloody stool.

Thermal simulations

Transient heat transfer FEA using the commercial software COMSOL 6.1 modelled the spatio-temporal temperature response of the implantable sensors to various physiological processes. A 2D model allowed extraction of the thermal profile and sensitivity of the sensor when placed near the surface of the normal and lesion regions of the intestines. Also, modelling the influence of vertical separation and horizontal misalignment between the intestinal lesions and the sensor enabled characterization of device sensitivity to the thermal fluctuations in the mouse and human anatomy. A parametric sweep captured the effect of changes in the thermal conductivity due to physiological processes in the intestines. The Pennes' bio-heat equation describes the heat transfer problem as[73,74]

$$\rho C_{\mathrm{p}} \frac{\partial mT}{\partial t} + \nabla \cdot (-k\nabla T) = \rho_{\mathrm{b}} C_{\mathrm{b}} \omega_{\mathrm{b}} (T_{\mathrm{b}} - T) + Q_{\mathrm{met}} \quad (1)$$

where T is temperature, t is time; k, ρ and C_{p} are the thermal conductivity, mass density and heat capacity of the tissues; and ρ_{b} and C_{b} are the effective mass density and specific heat capacity of the blood in the anatomical area near the intestines, respectively. $\omega_{\mathrm{b}} = 5.76 \times 10^{-3}\ \mathrm{m^3\ s^{-1}\ m^{-3}}$ denotes the blood perfusion rate, and $T_{\mathrm{b}} = 37\ ^{\circ}\mathrm{C}$ is the blood temperature. $Q_{\mathrm{met}} = 405.1\ \mathrm{W\ m^{-3}}$ is the heat source from metabolism in the intestines. A comprehensive list of thermal properties for body organs is given in ref. 75. The temperature profile of the normal intestines was modelled as a sine function over a 24 h period with a 1 °C amplitude between 35 °C and 37 °C. For the intestinal lesions, the thermal profile was modelled as a fourth-order polynomial to achieve two crests over the 24 h period. The temperature profiles were obtained with an output time step of 5 s in all cases. The total number of heat transfer elements used in the model is ~200,000. A mesh refinement was implemented to ensure accuracy. The thermal conductivity, heat capacity and density used in the model are 0.51 W m^{-1}, 3,680 J kg^{-1} K^{-1} and 1,085 kg m^{-3} for the skin layer; 0.23 W m^{-1}, 3,000 J kg^{-1} K^{-1} and 980 kg m^{-3} for the internal body; 0.47 W m^{-1}, 3,200 J kg^{-1} K^{-1} and 1,085 kg m^{-3} for the intestines; 3 W m^{-1}, 3,560 J kg^{-1} K^{-1} and 1,060 kg m^{-3} for the faeces; and 0.2 W m^{-1}, 1,090 J kg^{-1} K^{-1} and 1,420 kg m^{-3} for the sensor.

Statistical analysis and sample size

T-tests were conducted with JMP Pro software to compute *P* values. All *P* values reported throughout the manuscript and Supporting Information are two-sided. Minimum sample sizes for the experiments represented in Figs. 2d and 3e–i were determined using a power calculation with two independent study groups, continuous means, $\alpha = 0.05$ and power = 80%. All experiments involve more samples than the necessary minimum sample size computed from the power calculation. Figure 2d contains data on the initial $n = 1$ AKR/J and $n = 3$ SAMP1/YitFc animals used in this study for which blood collection did not coincide with a peak or valley in the $T_{\mathrm{intestines}}$ data, and hence these animals could not be included in Fig. 3e–h. Figure 3i contains data on additional control AKR/J mice for which sensors were not implanted. Because differences in serum biomarkers between the peak/valley or between strains were statistically significant in Fig. 3e–i, experiments with additional animals were not performed.

Reporting summary

Further information on research design is available in the Nature Portfolio Reporting Summary linked to this article.

Data availability

The main data supporting the results in this study are available within the paper and its Supplementary Information. Source data for Figs. 2d, 3b and 4f, as well as representative individual histology images used to produce Figs. 4g and 5d, are available with this paper. A larger number of additional individual histology images used to produce Figs. 4g and 5d are available from the corresponding authors on reasonable request. Source data are provided with this paper.

Code availability

Data analysis (spline fits, FFT, wavelet transform, peak/valley analysis, moving standard deviation) made use of inbuilt functions in MATLAB. All parameters used for analysis are available in Methods.

References

1. Jairath, V. & Feagan, B. G. Global burden of inflammatory bowel disease. *Lancet Gastroenterol. Hepatol.* **5**, 2–3 (2020).
2. Kaplan, G. G. & Windsor, J. W. The four epidemiological stages in the global evolution of inflammatory bowel disease. *Nat. Rev. Gastroenterol. Hepatol.* **18**, 56–66 (2021).
3. Kamm, M. A. Rapid changes in epidemiology of inflammatory bowel disease. *Lancet* **390**, 2741–2742 (2017).
4. Khor, B., Gardet, A. & Xavier, R. J. Genetics and pathogenesis of inflammatory bowel disease. *Nature* **474**, 307–317 (2011).
5. Torres, J., Mehandru, S., Colombel, J. F. & Peyrin-Biroulet, L. Crohn's disease. *Lancet* **389**, 1741–1755 (2017).
6. Santos, M. P. C., Gomes, C. & Torres, J. Familial and ethnic risk in inflammatory bowel disease. *Ann. Gastroenterol.* **31**, 14–23 (2018).

7. Goertz, R. S., Hensel, S., Wildner, D., Neurath, M. F. & Strobel, D. Bowel wall thickening and hyperemia assessed by high-frequency ultrasound indicate histological inflammation in Crohn's ileitis. *Abdom. Radiol.* **46**, 1855–1863 (2021).
8. Brown, E. & Taylor, C. T. Hypoxia-sensitive pathways in intestinal inflammation. *J. Physiol.* **596**, 2985–2989 (2018).
9. Li, J. et al. Dynamic role of macrophage CX3CR1 expression in inflammatory bowel disease. *Immunol. Lett.* **232**, 39–44 (2021).
10. Cushing, K. & Higgins, P. D. R. Management of Crohn disease: a review. *JAMA* **325**, 69–80 (2021).
11. Xiong, S. et al. Reverse translation approach generates a signature of penetrating fibrosis in Crohn's disease that is associated with anti-TNF response. *Gut* **71**, 1289–1301 (2022).
12. Hyun, J. G. et al. Anti-interferon-inducible chemokine, CXCL10, reduces colitis by impairing T helper-1 induction and recruitment in mice. *Inflamm. Bowel Dis.* **11**, 799–805 (2005).
13. Burgmann, T. et al. The Manitoba Inflammatory Bowel Disease Cohort Study: prolonged symptoms before diagnosis—how much is irritable bowel syndrome? *Clin. Gastroenterol. Hepatol.* **4**, 614–620 (2006).
14. Guglielmo, F. F. et al. Small bowel Crohn disease at CT and MR enterography: imaging atlas and glossary of terms. *Radiographics* **40**, 354–375 (2020).
15. Calabrese, E., Zorzi, F. & Pallone, F. Ultrasound of the small bowel in Crohn's disease. *Int J. Inflamm.* **2012**, 964720 (2012).
16. Stenczel, N. D., Purcarea, M. R., Tribus, L. C. & Oniga, G. H. The role of the intestinal ultrasound in Crohn's disease diagnosis and monitoring. *J. Med. Life* **14**, 310–315 (2021).
17. Yin, J. et al. The role of hypoxia-inducible factor 1-alpha in inflammatory bowel disease. *Cell Biol. Int.* **46**, 46–51 (2022).
18. Pizarro, T. T. et al. SAMP1/YitFc mouse strain: a spontaneous model of Crohn's disease-like ileitis. *Inflamm. Bowel Dis.* **17**, 2566–2584 (2011).
19. Bury, M. I. et al. Self-assembling nanofibers inhibit inflammation in a murine model of Crohn's-disease-like ileitis. *Adv. Therap.* **4**, 2000274 (2021).
20. Lucke, S. et al. Acute and chronic local inflammatory reaction after implantation of different extracellular porcine dermis collagen matrices in rats. *BioMed. Res. Int.* **2015**, 938059 (2015).
21. Schwerdt, H. N. et al. Long-term dopamine neurochemical monitoring in primates. *Proc. Natl Acad. Sci. USA* **114**, 13260–13265 (2017).
22. Chen, S. L. et al. The gut microbiota regulates acute foreign body reaction and tissue repair after biomaterial implantation. *Biomaterials* **289**, 121807 (2022).
23. Ellison, G. W., Case, J. B. & Regier, P. J. Intestinal surgery in small animals: historical foundations, current thinking, and future horizons. *Vet. Surg.* **48**, 1171–1180 (2019).
24. Doloff, J. C. et al. The surface topography of silicone breast implants mediates the foreign body response in mice, rabbits and humans. *Nat. Biomed. Eng.* **5**, 1115–1130 (2021).
25. Park, G. et al. Immunologic and tissue biocompatibility of flexible/stretchable electronics and optoelectronics. *Adv. Health. Mater.* **3**, 515–525 (2014).
26. Matsuzaki, K. et al. In vivo demonstration of T lymphocyte migration and amelioration of ileitis in intestinal mucosa of SAMP1/Yit mice by the inhibition of MAdCAM-1. *Clin. Exp. Immunol.* **140**, 22–31 (2005).
27. Lamont, E. W. & Amir, S. in *Encyclopedia of Behavioral Neuroscience* (eds Koob, G. F., Le Moal, M. & Thompson, R. F.) 257–261 (Academic Press, 2010).
28. Goh, G. H., Maloney, S. K., Mark, P. J. & Blache, D. Episodic ultradian events—ultradian rhythms. *Biology* 8 doi, 10.3390/biology8010015 (2019).
29. Smolensky, M. H., Hermida, R. C., Portaluppi, F., Haus, E. & Reinberg, A. in *Hypertension* 2nd edn (eds Oparil, S. & Weber, M.A.) 530–542 (W.B. Saunders, 2005).
30. Arts, L. P. A. & van den Broek, E. L. The fast continuous wavelet transformation (fCWT) for real-time, high-quality, noise-resistant time-frequency analysis. *Nat. Comput Sci.* **2**, 47–58 (2022).
31. Lou, H. & Ye, Z. [HRV signal analysis based on wavelet transform]. *Sheng Wu Yi Xue Gong. Cheng Xue Za Zhi* **23**, 21–24 (2006).
32. Addison, P. S. Wavelet transforms and the ECG: a review. *Physiol. Meas.* **26**, R155–R199 (2005).
33. Rankin, G. B. Extraintestinal and systemic manifestations of inflammatory bowel disease. *Med Clin. North Am.* **74**, 39–50 (1990).
34. Vavricka, S. R. et al. Extraintestinal manifestations of inflammatory bowel disease. *Inflamm. Bowel Dis.* **21**, 1982–1992 (2015).
35. Gordon, C. J. The mouse thermoregulatory system: its impact on translating biomedical data to humans. *Physiol. Behav.* **179**, 55–66 (2017).
36. Aschoff, J. Thermal conductance in mammals and birds—its dependence on body size and circadian phase. *Comp. Biochem Phys. A* **69**, 611–619 (1981).
37. Oh, S. et al. Simple, miniaturized biosensors for wireless mapping of thermoregulatory responses. *Biosens. Bioelectron.* **237**, 115545 (2023).
38. Atreya, R. et al. Blockade of interleukin 6 trans signaling suppresses T-cell resistance against apoptosis in chronic intestinal inflammation: evidence in Crohn disease and experimental colitis in vivo. *Nat. Med.* **6**, 583–588 (2000).
39. Atreya, R. et al. In vivo imaging using fluorescent antibodies to tumor necrosis factor predicts therapeutic response in Crohn's disease. *Nat. Med.* **20**, 313–318 (2014).
40. Langer, V. et al. IFN-gamma drives inflammatory bowel disease pathogenesis through VE-cadherin-directed vascular barrier disruption. *J. Clin. Invest.* **129**, 4691–4707 (2019).
41. Bouma, G. & Strober, W. The immunological and genetic basis of inflammatory bowel disease. *Nat. Rev. Immunol.* **3**, 521–533 (2003).
42. Mao, L., Kitani, A., Strober, W. & Fuss, I. J. The role of NLRP3 and IL-1beta in the pathogenesis of inflammatory bowel disease. *Front. Immunol.* **9**, 2566 (2018).
43. Liu, S., Russo, P. A., Baldassano, R. N. & Sullivan, K. E. CD68 expression is markedly different in Crohn's disease and the colitis associated with chronic granulomatous disease. *Inflamm. Bowel Dis.* **15**, 1213–1217 (2009).
44. Friedrich, M. et al. IL-1-driven stromal-neutrophil interactions define a subset of patients with inflammatory bowel disease that does not respond to therapies. *Nat. Med.* **27**, 1970–1981 (2021).
45. Padmanabhan, P., Grosse, J., Asad, A. B., Radda, G. K. & Golay, X. Gastrointestinal transit measurements in mice with 99mTc-DTPA-labeled activated charcoal using NanoSPECT-CT. *EJNMMI Res.* **3**, 60 (2013).
46. Rahman, M. M., Afroz, S., Arthur, S. & Sundaram, U. Mast cell mediated regulation of small intestinal chloride malabsorption in SAMP1/YitFc mouse model of spontaneous chronic ileitis. *Cells* https://doi.org/10.3390/cells10030697 (2021).
47. Gracie, D. J., Hamlin, P. J. & Ford, A. C. The influence of the brain–gut axis in inflammatory bowel disease and possible implications for treatment. *Lancet Gastroenterol. Hepatol.* **4**, 632–642 (2019).
48. Carabotti, M., Scirocco, A., Maselli, M. A. & Severi, C. The gut–brain axis: interactions between enteric microbiota, central and enteric nervous systems. *Ann. Gastroenterol.* **28**, 203–209 (2015).
49. Farhadi, A. et al. Heightened responses to stressors in patients with inflammatory bowel disease. *Am. J. Gastroenterol.* **100**, 1796–1804 (2005).

50. Vidrich, A. et al. Altered epithelial cell lineage allocation and global expansion of the crypt epithelial stem cell population are associated with ileitis in SAMP1/YitFc mice. *Am. J. Pathol.* **166**, 1055–1067 (2005).
51. Rivera-Nieves, J. et al. Emergence of perianal fistulizing disease in the SAMP1/YitFc mouse, a spontaneous model of chronic ileitis. *Gastroenterology* **124**, 972–982 (2003).
52. Daynes, R. A. & Jones, D. C. Emerging roles of PPARs in inflammation and immunity. *Nat. Rev. Immunol.* **2**, 748–759 (2002).
53. Wang, N. et al. Vascular PPARgamma controls circadian variation in blood pressure and heart rate through Bmal1. *Cell Metab.* **8**, 482–491 (2008).
54. Berger, J. P., Akiyama, T. E. & Meinke, P. T. PPARs: therapeutic targets for metabolic disease. *Trends Pharmacol. Sci.* **26**, 244–251 (2005).
55. Evans, R. M., Barish, G. D. & Wang, Y. X. PPARs and the complex journey to obesity. *Nat. Med.* **10**, 355–361 (2004).
56. Sugawara, K. et al. Linkage to peroxisome proliferator-activated receptor-gamma in SAMP1/YitFc mice and in human Crohn's disease. *Gastroenterology* **128**, 351–360 (2005).
57. Baumgart, D. C. & Sandborn, W. J. Crohn's disease. *Lancet* **380**, 1590–1605 (2012).
58. Favazzo, L. J. et al. The gut microbiome-joint connection: implications in osteoarthritis. *Curr. Opin. Rheumatol.* **32**, 92–101 (2020).
59. Arora, V. et al. Gut-microbiota modulation: the impact of the gut-microbiota on osteoarthritis. *Gene* **785**, 145619 (2021).
60. Sharma, S. et al. Location-aware ingestible microdevices for wireless monitoring of gastrointestinal dynamics. *Nat. Electron.* **6**, 242–256 (2023).
61. Tu, J. B. et al. A wireless patch for the monitoring of C-reactive protein in sweat. *Nat. Biomed. Eng.* https://doi.org/10.1038/s41551-023-01059-5 (2023).
62. Wagatsuma, K., Yokoyama, Y. & Nakase, H. Role of biomarkers in the diagnosis and treatment of inflammatory bowel disease. *Life* https://doi.org/10.3390/life11121375 (2021).
63. Chen, P. et al. Serum biomarkers for inflammatory bowel disease. *Front. Med.* **7**, 123 (2020).
64. Winogrodzki, T. et al. TNF DeltaARE pigs: a translational Crohn's disease model. *J. Crohns Colitis* **17**, 1128–1138 (2023).
65. Wanner, S. P., Costa, K. A., Soares, A. D., Cardoso, V. N. & Coimbra, C. C. Physical exercise-induced changes in the core body temperature of mice depend more on ambient temperature than on exercise protocol or intensity. *Int. J. Biometeorol.* **58**, 1077–1085 (2014).
66. Madhvapathy, S. R. et al. Implantable bioelectronic systems for early detection of kidney transplant rejection. *Science* **381**, 1105–1112 (2023).
67. Zhang, L. N. et al. Physiological and behavioral responses to intermittent starvation in C57BL/6J mice. *Physiol. Behav.* **105**, 376–387 (2012).
68. Severinsen, T. & Munch, I. C. Body core temperature during food restriction in rats. *Acta Physiol. Scand.* **165**, 299–305 (1999).
69. Kararli, T. T. Comparison of the gastrointestinal anatomy, physiology, and biochemistry of humans and commonly used laboratory animals. *Biopharm. Drug Dispos.* **16**, 351–380 (1995).
70. Casteleyn, C., Rekecki, A., Van der Aa, A., Simoens, P. & Van den Broeck, W. Surface area assessment of the murine intestinal tract as a prerequisite for oral dose translation from mouse to man. *Lab. Anim./* **44**, 176–183 (2010).
71. Yang, Q. et al. Photocurable bioresorbable adhesives as functional interfaces between flexible bioelectronic devices and soft biological tissues. *Nat. Mater.* **20**, 1559–1570 (2021).
72. Hwang, S. W. et al. A physically transient form of silicon electronics. *Science* **337**, 1640–1644 (2012).
73. Shih, T. C., Yuan, P., Lin, W. L. & Kou, H. S. Analytical analysis of the Pennes bioheat transfer equation with sinusoidal heat flux condition on skin surface. *Med. Eng. Phys.* **29**, 946–953 (2007).
74. Yang, Y. et al. Wireless multilateral devices for optogenetic studies of individual and social behaviors. *Nat. Neurosci.* **24**, 1035–1045 (2021).
75. Castellani, M. P., Rioux, T. P., Castellani, J. W., Potter, A. W. & Xu, X. A geometrically accurate 3 dimensional model of human thermoregulation for transient cold and hot environments. *Comput. Biol. Med.* **138**, 104892 (2021).

Acknowledgements

We thank F. Turek, M. Hotz-Vitaterna and K. Summa for useful discussions; M. Seniw (Simpson Querrey Institute, Northwestern University) for the illustrations in Fig. 1c; and H. M. Arafa, D. Ostojich and J.T. Williams for preliminary efforts in microfabrication and near-field communication device prototypes. This work made use of the MatCI Facility supported by the Materials Research Science and Engineering Center (MRSEC) program of the National Science Foundation (NSF) (DMR-1720139) at the Materials Research Center of Northwestern University, and of the micro/nano-fabrication (NUFAB) facility of Northwestern University's Atomic and Nanoscale Characterization Experimental Center, which has received support from the SHyNE Resource (NSF ECCS-2025633), the International Institute for Nanotechnology and Northwestern's MRSEC program. S.R.M and J.L.C. disclose support for the research described in this study from the NSF Graduate Research Fellowship Program (NSF DGE-2234667). The work was supported by the Querrey–Simpson Institute for Bioelectronics.

Author contributions

S.R.M., M.I.B., A.K.S. and J.A.R. conceived the project. S.R.M. designed the device hardware, software and encapsulation; fabricated devices; calibrated devices; conducted video analysis; and performed benchtop testing/characterization (with assistance from J.L.C.) and temperature data analysis. M.I.B. designed the surgical procedure and conducted surgeries, post-operative animal monitoring/care (with assistance from L.W.W.), motility measurements, histology sample preparation (with assistance from L.W.W.), analysis of quantitative histology (with assistance from L.W.W.), radiograph collection, video collection and blood collection/analysis. R.A. and Y.H. helped with thermal, electromagnetic and mechanical-modelling efforts associated with device operation. S.R.M. and M.I.B. performed data visualization. S.R.M., M.I.B., A.K.S. and J.A.R. analysed the data. S.R.M., M.I.B., A.K.S. and J.A.R. wrote the paper. All authors read and provided comments on the paper. J.A.R. and A.K.S. jointly supervised the work.

Competing interests

J.A.R., A.K.S., S.R.M., and M.I.B. are co-inventors on a patent related to the technology (US Patent App. 63/604,400) described in this work. The other authors declare no competing interests.

Additional information

Extended data is available for this paper at https://doi.org/10.1038/s41551-024-01183-w.

Supplementary information The online version contains supplementary material available at https://doi.org/10.1038/s41551-024-01183-w.

Correspondence and requests for materials should be addressed to Arun K. Sharma or John A. Rogers.

Peer review information *Nature Biomedical Engineering* thanks Jonathan Cooper, Wei Gao and Taeyoon Lee for their contribution to the peer review of this work. Peer reviewer reports are available.

https://doi.org/10.1038/s41551-024-01183-w

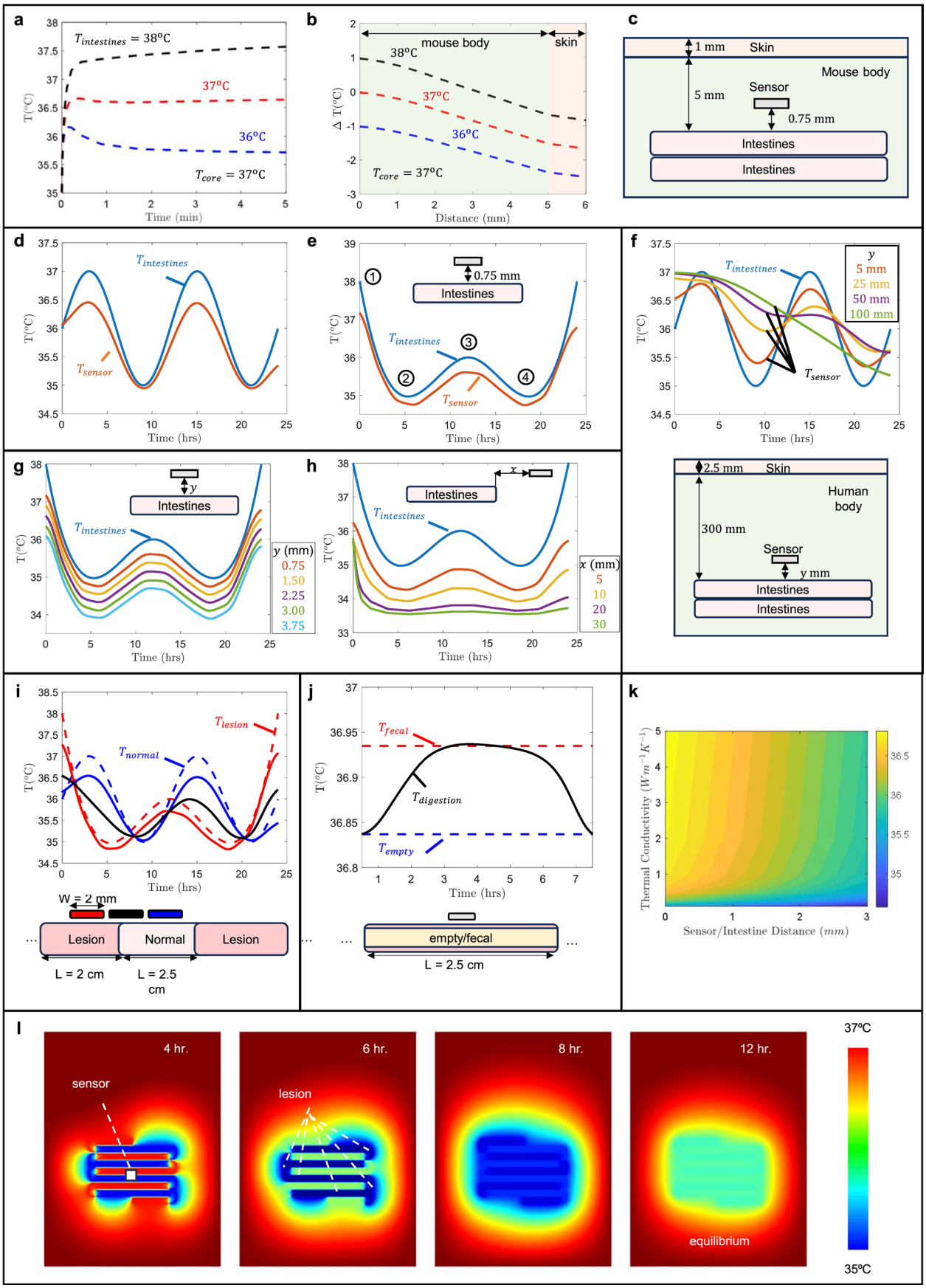

Extended Data Fig. 1 | See next page for caption.

https://doi.org/10.1038/s41551-024-01183-w

Extended Data Fig. 1 | FEA modeling of the temperature sensitivity of the device to temperature fluctuations in the intestines. (a) Temperature profile in the sensor over a 5-hour period to reach steady state temperature when the temperature of the intestines increases by 1 °C (black), remains the same 0 °C (red), and decreases by 1 °C (blue) with respect to the body temperature. The core body temperature was fixed at 37 °C. **(b)** Steady state temperature change ($\Delta T = T_{intestines} - T_{core}$) profile between the surface of the intestines and the outer skin layer in a mouse for the three cases in (a); the distance between the intestines and skin is assumed to be 5 mm and the thickness of the skin layer is 1 mm. **(c)** FEA model for (a,b). **(d)** Sinusoidal temperature profile at the surface of the intestines over a 24-hr period and the corresponding temperature profile in the temperature sensors showing excellent agreement by capturing the thermal fluctuations. **(e)** A 4th order polynomial temperature profile at the surface of the 'lesion' intestines over a 24-hr period and the corresponding temperature profile in the temperature sensors showing excellent agreement by capturing the thermal fluctuations. In both (d,e), the distance between the sensor and intestines is 0.75 mm. **(f)** (Top) Temperature profile in the sensor as the vertical separation distance between the surface of the intestines and sensor increases from 5 mm to 100 mm, modeling the scenario in a human. The temperature in the intestines is modeled as a sinusoidal wave. As the vertical separation distance increases to 50 mm and 100 mm the sensor is unable to pick up the thermal fluctuations in the intestines. (Bottom) Schematic of the FEA model. **(g)** Temperature profiles in the sensor as a function of time when the vertical distance between the sensor increases from 0.75 mm to 3.75 mm showing that for all cases the sensor can capture the 4th order polynomial profile of the intestines. **(h)** Temperature profiles in the sensor as a function of time when the horizontal distance, or lateral misalignment, between the sensor increases from 5 mm to 30 mm. For the cases when the sensor is 20 mm and 30 mm away from the edge of the intestines the sensor is unable to capture the thermal fluctuations at the surface of the intestines. **(i)** (Top) Thermal profiles for the sensor when placed on top of the lesion region (solid red), normal region (solid blue), and between lesion and normal region (solid black). The thermal profiles are a sinusoidal wave for the normal intestine (dashed blue) and 4th order polynomial for the lesion intestine (dashed red). (Bottom) Schematic of the arrangement for the lesion intestines, normal intestines, and the sensor placement. **(j)** (Top) Steady state temperature limits at the sensor when the intestine is empty (dashed blue) and with fecal matter (dashed red). The black curve shows the thermal profile when fecal matter enters (temperature increases) and leaves (temperature decreases) the intestine over a period of 8 hrs. (Bottom) Schematic of the model showing the difference between the internal part of the intestine for the empty/fecal cases. **(k)** Surface plot of the steady state temperature in the sensor based on a parametric sweep of the distance between the sensor and intestine (horizontal axis) and the thermal conductivity of the intestines (vertical axis). **(l)** Transient heat transfer process over a 12-hr process to reach thermal equilibrium in the intestine's region.

https://doi.org/10.1038/s41551-024-01183-w

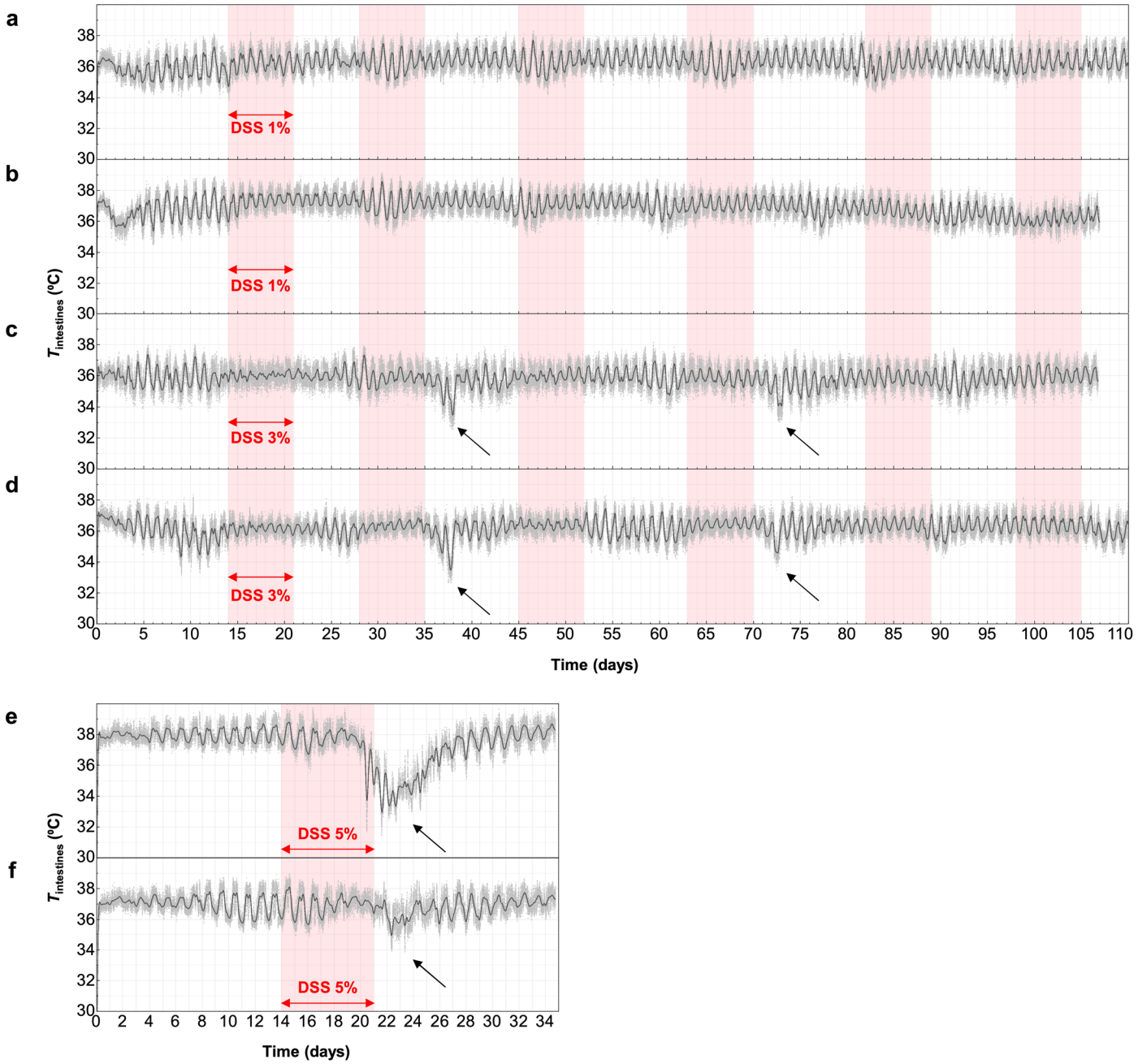

Extended Data Fig. 2 | A DSS-induced model of colitis. $T_{intestines}$ as a function of time for individual AKR/J mice subject to intermittent administration of **(a, b)** 1% and **(c, d)** 3% by volume DSS in the drinking water over 107–110 days. The red shaded regions indicate the time period for which DSS was administered. Animals were killed on day 107 in panels (b, c) and day 110 in panels (a, d). **(e, f)** $T_{intestines}$ as a function of time for individual mice subject to 5% by volume of DSS in the drinking water. The red shaded region indicates the time window for which DSS was administered. Animals were euthanized on day 35. The black arrows in all panels indicate a significant drop in $T_{intestines}$ after administration of DSS, if applicable.

nature portfolio

Corresponding author(s): John A. Rogers, Arun K. Sharma

Last updated by author(s): Feb 8, 2024

Reporting Summary

Nature Portfolio wishes to improve the reproducibility of the work that we publish. This form provides structure for consistency and transparency in reporting. For further information on Nature Portfolio policies, see our Editorial Policies and the Editorial Policy Checklist.

Statistics

For all statistical analyses, confirm that the following items are present in the figure legend, table legend, main text, or Methods section.

n/a	Confirmed
☐	☒ The exact sample size (*n*) for each experimental group/condition, given as a discrete number and unit of measurement
☐	☒ A statement on whether measurements were taken from distinct samples or whether the same sample was measured repeatedly
☐	☒ The statistical test(s) used AND whether they are one- or two-sided *Only common tests should be described solely by name; describe more complex techniques in the Methods section.*
☐	☒ A description of all covariates tested
☒	☐ A description of any assumptions or corrections, such as tests of normality and adjustment for multiple comparisons
☐	☒ A full description of the statistical parameters including central tendency (e.g. means) or other basic estimates (e.g. regression coefficient) AND variation (e.g. standard deviation) or associated estimates of uncertainty (e.g. confidence intervals)
☐	☒ For null hypothesis testing, the test statistic (e.g. *F*, *t*, *r*) with confidence intervals, effect sizes, degrees of freedom and *P* value noted *Give P values as exact values whenever suitable.*
☒	☐ For Bayesian analysis, information on the choice of priors and Markov chain Monte Carlo settings
☒	☐ For hierarchical and complex designs, identification of the appropriate level for tests and full reporting of outcomes
☒	☐ Estimates of effect sizes (e.g. Cohen's *d*, Pearson's *r*), indicating how they were calculated

Our web collection on statistics for biologists contains articles on many of the points above.

Software and code

Policy information about availability of computer code

Data collection	TeraTerm and Keil Microvision (BLE SoC firmware).
Data analysis	JMP Pro 16, Matlab 2022b and DeepLabCut.

For manuscripts utilizing custom algorithms or software that are central to the research but not yet described in published literature, software must be made available to editors and reviewers. We strongly encourage code deposition in a community repository (e.g. GitHub). See the Nature Portfolio guidelines for submitting code & software for further information.

Data

Policy information about availability of data

All manuscripts must include a data availability statement. This statement should provide the following information, where applicable:

- Accession codes, unique identifiers, or web links for publicly available datasets
- A description of any restrictions on data availability
- For clinical datasets or third party data, please ensure that the statement adheres to our policy

The main data supporting the results in this study are available within the paper and its Supplementary Information. Source data for Figs. 2d, 3b and 4f, as well as representative Individual histology images used to produce Fig. 4g and 5d, are available with this paper. A larger number of additional individual histology images used to produce Fig. 4g and 5d are available from the corresponding authors on reasonable request.

Research involving human participants, their data, or biological material

Policy information about studies with human participants or human data. See also policy information about sex, gender (identity/presentation), and sexual orientation and race, ethnicity and racism.

Reporting on sex and gender	The study did not involve human participants.
Reporting on race, ethnicity, or other socially relevant groupings	–
Population characteristics	–
Recruitment	–
Ethics oversight	–

Note that full information on the approval of the study protocol must also be provided in the manuscript.

Field-specific reporting

Please select the one below that is the best fit for your research. If you are not sure, read the appropriate sections before making your selection.

☒ Life sciences ☐ Behavioural & social sciences ☐ Ecological, evolutionary & environmental sciences

For a reference copy of the document with all sections, see nature.com/documents/nr-reporting-summary-flat.pdf

Life sciences study design

All studies must disclose on these points even when the disclosure is negative.

Sample size	The minimum sample size was determined using a power calculation with two independent study groups, continuous means, alpha = 0.05, and power = 80%.
Data exclusions	No data were excluded from the analyses.
Replication	Animal experiments were replicated multiple times (as indicated in each figure caption) and sensors were tested/calibrated multiple times (at least 3 technical replicates per sensor).
Randomization	The animals were randomly assigned to experimental groups.
Blinding	The investigators were blinded to group allocation for quantitative and qualitative histological scoring.

Reporting for specific materials, systems and methods

We require information from authors about some types of materials, experimental systems and methods used in many studies. Here, indicate whether each material, system or method listed is relevant to your study. If you are not sure if a list item applies to your research, read the appropriate section before selecting a response.

Materials & experimental systems

n/a	Involved in the study
☒	☐ Antibodies
☒	☐ Eukaryotic cell lines
☒	☐ Palaeontology and archaeology
☐	☒ Animals and other organisms
☒	☐ Clinical data
☒	☐ Dual use research of concern
☒	☐ Plants

Methods

n/a	Involved in the study
☒	☐ ChIP-seq
☒	☐ Flow cytometry
☒	☐ MRI-based neuroimaging

Animals and other research organisms

Policy information about studies involving animals; ARRIVE guidelines recommended for reporting animal research, and Sex and Gender in Research

Laboratory animals	SAMP1/YitFc mice (The Jackson Laboratory, USA) aged 4–20 weeks and female AKR/J mice aged 12–20 weeks (The Jackson Laboratory, USA) formed the experimental and control groups, respectively.
Wild animals	The study did not involve wild animals.
Reporting on sex	All animals were female, and sex was not considered in the design of the study. Sex was assigned through the vendor (The Jackson Laboratory).
Field-collected samples	The study did not involve samples collected from the field.
Ethics oversight	The Institutional Animal Care and Use Committee (IACUC) at Northwestern University's Center for Comparative Medicine (CCM) approved all animals and procedures prior to experimentation (IS12661).

Note that full information on the approval of the study protocol must also be provided in the manuscript.